AGU PUBLICATIONS

JGR

Journal of Geophysical Research: Space Physics

RESEARCH ARTICLE

10.1002/2016JA022701

Solar cycle variability in mean thermospheric composition and temperature induced by atmospheric tides

M. Jones Jr.[1], J. M. Forbes[2], and M. E. Hagan[3]

[1]National Research Council Post Doctoral Fellow, Space Sciences Division, U.S. Naval Research Laboratory, Washington, District of Columbia, USA, [2]Department of Aerospace Engineering Sciences, University of Colorado Boulder, Boulder, Colorado, USA, [3]Department of Physics, Utah State University, Logan, Utah, USA

Key Points:
- Zonal-mean temperature differences induced by the dissipating tides vary considerably with solar cycle
- The solar cycle variability in tidal-induced zonal-mean temperature changes result from tidally driven increases in nitric oxide cooling
- Through tidal-induced temperature and constituent changes, tidal modifications to the ionosphere are quite substantial

Correspondence to:
M. Jones Jr.,
mcarthur.jones.ctr@nrl.navy.mil

Citation:
Jones, M. Jr., J. M. Forbes, and M. E. Hagan (2016), Solar cycle variability in mean thermospheric composition and temperature induced by atmospheric tides, *J. Geophys. Res. Space Physics*, *121*, 5837–5855, doi:10.1002/2016JA022701.

Received 15 MAR 2016
Accepted 4 JUN 2016
Accepted article online 10 JUN 2016
Published online 28 JUN 2016

Abstract In this paper we demonstrate that dissipation of upward propagating tides produces significant changes in the mean temperature of the thermosphere, ranging from +19 K at solar minimum to −15 K at solar maximum in the equatorial region. Our methodology consists of measuring the differential response of the thermosphere-ionosphere-electrodynamics general circulation model (TIE-GCM) under solar minimum and solar maximum conditions to constant tidal forcing at its 97 km lower boundary, as specified by the observationally based Climatological Tidal Model of the Thermosphere. Diagnosis of the model reveals that these changes are mainly driven by 5.3 μm nitric oxide (NO) cooling, which more efficiently cools the thermosphere at solar maximum. The main role of the tides is to modify the mean molecular oxygen densities ($[O_2]$) through tidal-induced advective transport, which then lead to changes in NO densities through oxygen-nitrogen chemistry. Through tidal-induced changes in temperature and O, O_2, and N_2 densities, effects on the ionosphere are also quite substantial; tidal-induced modifications to zonal-mean *F* region peak electron densities (N_mF_2) are of order −10% at solar maximum and −30% at solar minimum in the equatorial region. Our results introduce an additional consideration when attributing long-term changes in thermospheric temperature and electron densities to CO_2 cooling effects alone; that is, dissipation of upward propagating tides may constitute an additional element of global change in the ionosphere-thermosphere (IT) system.

1. Introduction

Understanding the different processes contributing to the energy budget of the ionosphere-thermosphere (IT) system is fundamental to understanding its thermal, dynamical, and compositional structure. This understanding furthermore underlies achievement of more accurate space weather forecasts in support of tracking and monitoring near-Earth orbiting satellites and space debris [e.g., *Leonard et al.*, 2012; *Emmert*, 2015]. The majority of the energy available to the IT system comes from above, through the absorption of extreme ultraviolet (EUV) and ultraviolet (UV) solar radiation; however, the absorption of solar radiation in the lower atmosphere supplies additional energy to the thermosphere through the dissipation of upward propagating tides and gravity waves. The dynamical upward transport of energy due to thermal tides is in fact a regular and repeatable energy source within the IT system. Recently, numerous studies [*Talaat and Lieberman*, 1999; *Oberheide et al.*, 2002; *Forbes and Wu*, 2006; *Forbes et al.*, 2006; *Zhang et al.*, 2006; *Forbes et al.*, 2008, 2009; *Friedman et al.*, 2009; *Mukhtarov et al.*, 2009; *Oberheide et al.*, 2009; *Xu et al.*, 2009; *Pancheva et al.*, 2010; *Zhang et al.*, 2010a, 2010b; *Oberheide et al.*, 2011a; *Truskowski et al.*, 2014; *Li et al.*, 2015] report on the climatology, global structure, and variability associated with tides in the thermosphere, and yet the effects of their dissipation on the IT system have received relatively little attention over the last 50 years.

Initial modeling studies by *Hines* [1965] and *Lindzen* [1967] showed that internal gravity waves and atmospheric tides transport energy vertically from the lower atmosphere into the IT and affect the energy budget of the IT once they are dissipated via eddy heat flux divergence. *Lindzen and Blake* [1970] stated that the heat transport arising from semidiurnal (12 h) tidal dissipation is extremely important in maintaining exospheric temperatures. *Groves and Forbes* [1984, 1985] also reported that diurnal (24 h) and semidiurnal tidal dissipation can lead to globally averaged energy inputs comparable to the daily-averaged EUV absorption in the lower thermosphere. In the early 1990s, *Forbes et al.* [1993] utilized the National Center for Atmospheric Research (NCAR) thermosphere-ionosphere general circulation model (TIGCM) [e.g., *Roble et al.*, 1988] and reported that

dissipation of the migrating (i.e., Sun-synchronous) diurnal and semidiurnal tides alter the zonally and diurnally averaged temperatures by −5 to +8 K in the IT. Contrary to previously published works, they concluded that tidal dissipation was not a significant contributor to the thermal energy budget of the thermosphere.

Other than direct tidal heating via eddy heat flux divergence, tidal dissipation could potentially contribute to the energy budget of the IT system through changes in the mean circulation (i.e., adiabatic heating and cooling) or changes in the density of neutral atmospheric constituents (e.g., O, O_2, N_2, NO, and CO_2), which determine radiative cooling rates and heating rates due solar radiation absorption or heating due to exothermic chemical reactions. *Akmaev and Shved* [1980], *Forbes et al.* [1993], *Smith et al.* [2010], *Yamazaki and Richmond* [2013], and *Jones et al.* [2014a, 2014b] all report changes in the major neutral constituents driven by tidal-induced processes, which could affect the energy budget of the IT either through the absorption of solar radiation, or by radiating themselves. *Marsh and Russell* [2000] and *Marsh and Roble* [2002] reported that daily and seasonal nitric oxide (NO) variability from the halogen occultation experiment (HALOE) measurements resulted from tidal vertical motions in the lower thermosphere. NO cooling is known to significantly contribute to the energy budget of the thermosphere [e.g., *Kockarts*, 1980; *Mlynczak et al.*, 2003]. More recently, *Oberheide and Forbes* [2008], *Ren et al.* [2011], and *Oberheide et al.* [2013] all demonstrated that significant longitudinal variability in NO (and thus infrared cooling) is induced by nonmigrating tides, thus reinforcing the notion that NO is responsive to tidal dynamics.

Many of these different tidal effects on the IT energy budget could also have a strong solar cycle dependence. For example, *Oberheide et al.* [2009] and references therein show that tidal dissipation becomes more important as solar activity increases; i.e., smaller (larger) neutral density leads to reduced (increased) dissipation during solar cycle minimum (maximum). This could potentially impact the altitudes at which the tides dissipate and subsequently deposit heat into the background IT via eddy heat flux divergence. *Forbes* [1978] showed that tidal amplitude variations in major (O, O_2, and N_2) and minor (Ar, He, and H) thermospheric constituents were solar cycle dependent, potentially indicating that there is solar cycle variability associated with atmospheric tidal effects on the energy budget of the IT. Moreover, *Mlynczak et al.* [2010, 2014] reported that NO (and CO_2) infrared radiative (IR) cooling in the thermosphere has a strong solar cycle dependence, implying that the tidal effects described by *Oberheide and Forbes* [2008], *Ren et al.* [2011], and *Oberheide et al.* [2013] on the NO IR cooling could modulate its inherent solar cycle behavior.

All the studies discussed above motivate this current work, which seeks to better understand to what extent the dissipation of atmospheric tides contributes to the zonally and diurnally averaged (or the longitude and time means, hereafter referred to as "zonal mean") thermal energy budget of the IT system. Toward this end, we employ the NCAR thermosphere-ionosphere-electrodynamics general circulation model (TIE-GCM) to address this topic by performing a series of numerical experiments using observationally based background (i.e., zonally and diurnally averaged) and tidal lower boundary conditions [after *Jones et al.*, 2014a]. We quantify and identify the different tidal-induced mechanisms responsible for maintaining the zonal-mean thermal energy budget of the IT system by calculating differences in the individual forcing terms of the thermodynamic energy equation between simulations including and excluding lower boundary tidal forcing. Furthermore, solar cycle dependencies associated with these tidal impacts on the zonal-mean temperature structure of the thermosphere are evaluated from TIE-GCM simulations under solar minimum, medium, and maximum conditions. Results presented herein are considered and discussed in light of the aforementioned research efforts, as well as quantified relative to the inherent solar cycle variability associated with IT system parameters.

2. TIE-GCM Simulations and Methodology

The NCAR TIE-GCM is a physics-based numerical general circulation model extending from ~97 km to ~600–750 km (depending on solar cycle) designed to self-consistently simulate the dynamics, thermodynamics, electrodynamics, and chemistry of the IT system from first-principles for a predetermined set of solar irradiance values (i.e., using a 10.7 cm solar radio flux ($F_{10.7}$)) and geomagnetic proxies (hemispheric power value after [*Evans*, 1987] and cross-cap potential drop). The reader is referred to *Dickinson et al.* [1981, 1984], *Roble et al.* [1988], *Richmond et al.* [1992], *Wang* [1998], *Qian* [2013], and *Richmond and Maute* [2014] for a more comprehensive description of the model physics, as well as the historical development of the TIE-GCM.

TIE-GCM simulations reported on herein were performed using version 1.94 of the model at a horizontal resolution of 2.5° × 2.5° (longitude × latitude) and a vertical resolution of 4 points per scale height. September

climatologies were simulated by running the TIE-GCM for the fifteenth day of the month (i.e., day of year 258) until the model reached a diurnally reproducible state. To elucidate the solar cycle variability associated with tidal dissipation in the IT solar minimum, medium, and maximum conditions were simulated using $F_{10.7}$ values of 75, 120, and 200 sfu (10^{-22} W m^{-2} Hz^{-1}), respectively, and these $F_{10.7}$ values were held constant throughout the entire model run. Geomagnetic quiescent conditions were replicated by using a hemispheric power value of 8 GW, and cross-cap potential drop of 30 kV, and these values were also held constant in all of our simulations. Like the TIE-GCM simulations performed by *Jones et al.* [2014a], we multiplied the TIE-GCM solar fluxes in the 8–70 Å range by a factor of 4.4 [after *Fang et al.*, 2008] in order to more realistically simulate *E* region electrodynamics. The sensitivity of our results to this assumption is discussed in section 3.3.

We utilized observationally based background (or zonal mean) and tidal lower boundary conditions that are identical to those described in detail by *Jones et al.* [2014a]. Considering that this study is focused on interpreting the tidal effects on the thermal energy budget of the IT system, we briefly summarize the tidal lower boundary conditions employed in our TIE-GCM simulations. Atmospheric tides produced in situ in the IT via UV and EUV solar radiation absorption are inherently accounted for in the TIE-GCM. Migrating and nonmigrating diurnal and semidiurnal tidal perturbations (with zonal wave numbers between ±6) generated in the troposphere, stratosphere, and mesosphere from the Climatological Tidal Model of the Thermosphere (CTMT) [see *Oberheide et al.*, 2011b] are introduced as model lower boundary conditions. To determine the tidal-induced changes on the zonal-mean thermal energy budget of the IT, differences between TIE-GCM runs including CTMT tidal forcing with those either including only specific tidal components, or removing CTMT tidal forcing altogether (i.e., only the zonal-mean wind, temperature, and geopotential height fields are forced) under varying solar cycle conditions, are evaluated. Furthermore, differences in the forcing terms of the thermodynamic energy equation are analyzed to establish the dominant physical mechanisms responsible for modifying the zonal-mean thermal balance of the IT and the solar cycle variability associated with these mechanisms.

3. Result and Discussion

3.1. Tidal Impacts on the Zonal-Mean Temperature

Figure 1 depicts the zonal-mean temperature differences induced by tidal dissipation as a function of latitude, altitude, and solar cycle from the TIE-GCM. Differences between results including and excluding CTMT tidal forcing (hereafter referred to as "with/without TBCs") are shown in the first row of Figure 1 under solar minimum (Figure 1a), medium (Figure 1b), and maximum conditions (Figure 1c) during September. We chose to present TIE-GCM results from the month of September because the tides exert their largest influence on the zonal-mean temperatures in our TIE-GCM simulations around the equinoxes (not shown) and also because the tidal forcing from the lower atmosphere is at or near its maximum [e.g., *Zhang et al.*, 2006; *Forbes et al.*, 2008; *Oberheide et al.*, 2009, 2011b]. Furthermore, the results illustrated in Figure 1 for September are representative of the tidal effects on the zonal-mean temperatures at equinox (i.e., analogous tidal impacts on the zonal-mean temperatures are calculated during March and therefore not shown). Vertically propagating tides affect the zonal-mean temperatures of the thermosphere over all levels of solar activity with maximum (minimum) differences of +19 K (−15 K) occurring over the equator (±30° latitude) under solar minimum (maximum) conditions. The +19 K increase in zonal-mean temperature centered over the equator at solar minimum induced by the dissipating tides (Figure 1a) is reduced as solar activity increases, only reaching +6 K at solar medium (Figure 1b), and eventually a minimum of −8 K at solar maximum (Figure 1c). Essentially, the effect of tidal dissipation on the zonal-mean temperature of the thermosphere depends on solar cycle; i.e., during solar minimum there is a net increase in zonal-mean temperature at equatorial latitudes, while during solar maximum tidal dissipation leads to a decrease in zonal-mean temperature at equatorial latitudes. Similar behavior (i.e., zonal-mean temperature differences decreasing with increasing solar activity) in the zonal-mean temperature changes driven by the tides is also depicted in Figures 1a–1c at latitudes poleward of the equator. The one consistent feature in the zonal-mean temperature differences depicted in Figures 1a–1c is the +2 to +4 K increase in the zonal-mean temperature differences below ~110 km, which tend to move southward as solar activity increases.

The spatial structure and magnitude of the zonal-mean temperature changes induced by tidal dissipation illustrated in Figure 1b are consistent with those calculated by *Forbes et al.* [1993], who only considered migrating diurnal and semidiurnal tides at the TIGCM lower boundary. Thus, we revaluate the relative importance of the tidal components most responsible for altering the zonal-mean temperature structure of the IT system

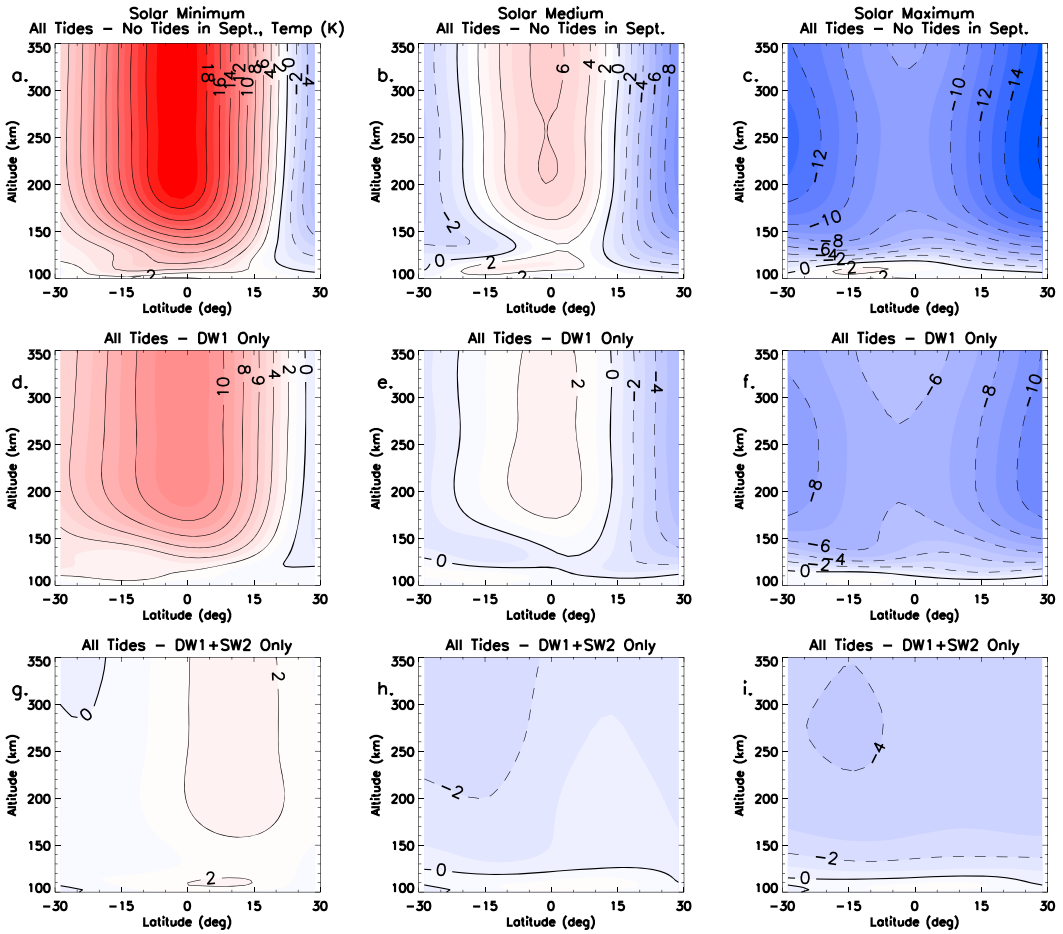

Figure 1. Zonal-mean temperature differences between TIE-GCM simulations under different CTMT tidal lower boundary and solar cycle conditions during the month of September as a function of latitude and altitude. Differences computed from TIE-GCM simulations under solar (a, d, and g) minimum, (b, e, and h) medium, and (c, f, and i) maximum conditions are shown. Differences computed between TIE-GCM simulations including and excluding CTMT tidal lower boundary forcing are shown (Figures 1a–1c); differences between TIE-GCM simulations including all tidal components and only the DW1 from CTMT at the model lower boundary are shown (Figures 1d–1f); and differences between TIE-GCM simulations including all tidal components and only the DW1 and SW2 from CTMT at the model lower boundary are shown (Figures 1g–1i). Zonal-mean temperature differences are contoured every ±2 K.

by computing difference fields between TIE-GCM simulations including CTMT lower boundary tidal forcing with TIE-GCM simulations that include only a linear combination of specific tidal components from the CTMT. Figures 1d–1f show the differences between simulations that include all of the CTMT tidal components forced at the model lower boundary and simulations that only include tidal forcing from the migrating diurnal tide with zonal wave number 1 (DW1) as a function of latitude, altitude, and solar cycle. By including just DW1, the mean temperature differences are reduced by ~40–50% under solar minimum and medium conditions at low latitudes (Figures 1d and 1e). Under solar maximum conditions DW1 has a smaller effect, only accounting for at most −4 K (or ~25–35%) changes in the zonal-mean temperature (Figure 1f).

Including the migrating semidiurnal tide with zonal wave number 2 (SW2) with the DW1 at the TIE-GCM lower boundary explains the majority of the zonal-mean temperature differences in the IT at all levels of solar activity (Figures 1g–1i). Specifically, mean temperature differences ranging from −1 to +10 K, −5 to +2 K, and −11 to +1 K under solar minimum, medium, and maximum conditions, respectively, that are unaccounted for by the DW1 in Figures 1d–1f are reduced to −4 to +2 K at all levels of solar activity by considering both migrating tidal components (Figures 1g–1i). The results shown in Figures 1d–1i lead us to conclude that the migrating tides explain at least 70% of the zonal-mean temperature differences in the TIE-GCM regardless of solar cycle. Therefore, our remaining interpretation of the different mechanisms responsible for driving the solar cycle

variability in the zonal-mean temperature differences calculated from the TIE-GCM will be ascribed to the migrating tides, with the nonmigrating playing a secondary role.

3.2. Diagnosing the Solar Cycle Variability in Zonal-Mean Temperature

Diagnosing the mechanisms by which the tides act to change the zonal-mean temperature is facilitated by calculating each individual term of the thermodynamic energy equation and quantifying their changes due to the presence of the tides in the TIE-GCM as a function of solar cycle. To obtain this equation, we decompose the dependent variables (e.g., temperature, winds, diabatic, and heating) in the full thermodynamic energy equation into zonal-mean quantities varying only in latitude and altitude, and perturbation (tidal) quantities depending on all three spatial dimensions and time. Assuming Earth's atmosphere is in hydrostatic equilibrium and following *Dickinson et al.* [1975] and *Holton* [1975], we subsequently calculate longitudinal and temporal means to arrive at the zonal-mean form of the equation in height and spherical coordinates:

$$\frac{\overline{v}}{a}\frac{\partial \overline{T}}{\partial \theta} + \overline{w}\overline{S} = \frac{\overline{J}}{c_{p_0}} - \overline{G} + \frac{1}{\rho_0 c_{p_0}}\frac{\partial}{\partial z}\left[\overline{K_T}\frac{\partial \overline{T}}{\partial z} + \overline{K_E}\rho_0 c_{p_0}\left(\frac{g}{c_{p_0}} + \frac{\partial \overline{T}}{\partial z}\right)\right], \tag{1}$$

where the terms with overbars represent the zonal-mean quantities. The variables in equation (1) are as follows: θ = latitude, z = altitude, a = radius of the Earth, g = gravity, c_{p0} = basic state specific heat at constant pressure, ρ_0 = basic state density, T = temperature, v = meridional wind velocity, w = vertical wind velocity, K_T = thermal conductivity, K_E = eddy diffusion coefficient, J = diabatic heating rate, S = static stability, and G = eddy heat source term. The static stability and eddy heat source term are defined following *Dickinson et al.* [1975] and *Holton* [1975]:

$$\overline{S} = \left(\frac{\partial \overline{T}}{\partial z} + \frac{\kappa \overline{T}}{H}\right),$$

$$\overline{G} \equiv \frac{1}{a\cos\theta}\frac{\partial}{\partial \theta}\left(\overline{v'T'}\cos\theta\right) + \frac{1}{\rho_0}\frac{\partial}{\partial z}\left(\rho_0 \overline{w'T'}\right) + \frac{R}{\overline{m}c_{p_0}H}\overline{w'T'},$$

where the prime terms represent the perturbations or tides (i.e., residuals from the zonal-mean quantities), R is the universal gas constant, $\overline{m}$ is the mean molecular weight, H is the mean scale height, and $\kappa = \frac{R}{c_p}$. The first term on the left-hand side of equation (1) is the meridional temperature advection term, and the second term on the left-hand side of equation (1) is the adiabatic heating and cooling term (or Adia. H/C representing changes in temperature as an air parcel is moved vertically). The first term on the right-hand side of equation (1) is the diabatic heating and cooling term (or Dia. H/C). The diabatic heating rate (J) represents the differences in the diabatic heat sources (Q) and sinks (L). Diabatic heat sources in the TIE-GCM include radiative heating, joule heating, heating due to oxygen (O) recombination, heating due to molecular diffusion, and heating due to numerical diffusion. Diabatic cooling terms in the TIE-GCM result from 5.3 μm NO, 15 μm carbon dioxide (CO_2), and 63 μm $O(^3P)$ IR radiative cooling. The second term on the right-hand side of equation (1) is the eddy heat source term (or Eddy Heat), which represents the deposition of heat (energy) by the dissipating tides. The final term on the right-hand side of equation (1) is the dissipative term that includes both vertical molecular heat conduction (thermal conductivity) and eddy diffusion of heat. The effects of eddy conductivity on the zonal-mean temperature are largest within the first two model scale heights (i.e., the TIE-GCM lower boundary is situated at ~97 km), above which the thermal conductivity term becomes the dominant dissipative term in the TIE-GCM.

To understand how the dissipating tides (i.e., mainly the migrating tides) act to induce solar cycle dependency in the zonal-mean temperature differences illustrated in Figure 1, differences in the Adia. H/C term, Eddy Heat, Dia. H/C terms, and their sum from TIE-GCM simulations with/without TBCs under solar minimum and maximum conditions are presented in Figure 2. Because the zonal-mean temperature differences depicted in Figures 1a–1c are fairly constant with altitude above ~200 km due to molecular conduction, Figure 2 only illustrates results limited to the 100–200 km height regime, recognizing that differences in the zonal-mean temperatures mainly occur at lower thermospheric altitudes where the neutral density is largest. Furthermore, the differences induced by the dissipating tides on the advective and dissipative terms are small relative to the other terms and therefore are not shown in Figure 2. Figures 2a and 2b show adiabatic heating and cooling differences ranging from about ±30 K d^{-1} at low latitudes and lower thermospheric altitudes driven by tidal dissipation, during both solar minimum and maximum. Differences in the Eddy Heat term shown in Figures 2c and 2d display the opposite latitudinal structure (i.e., latitudinal structure of the maxima

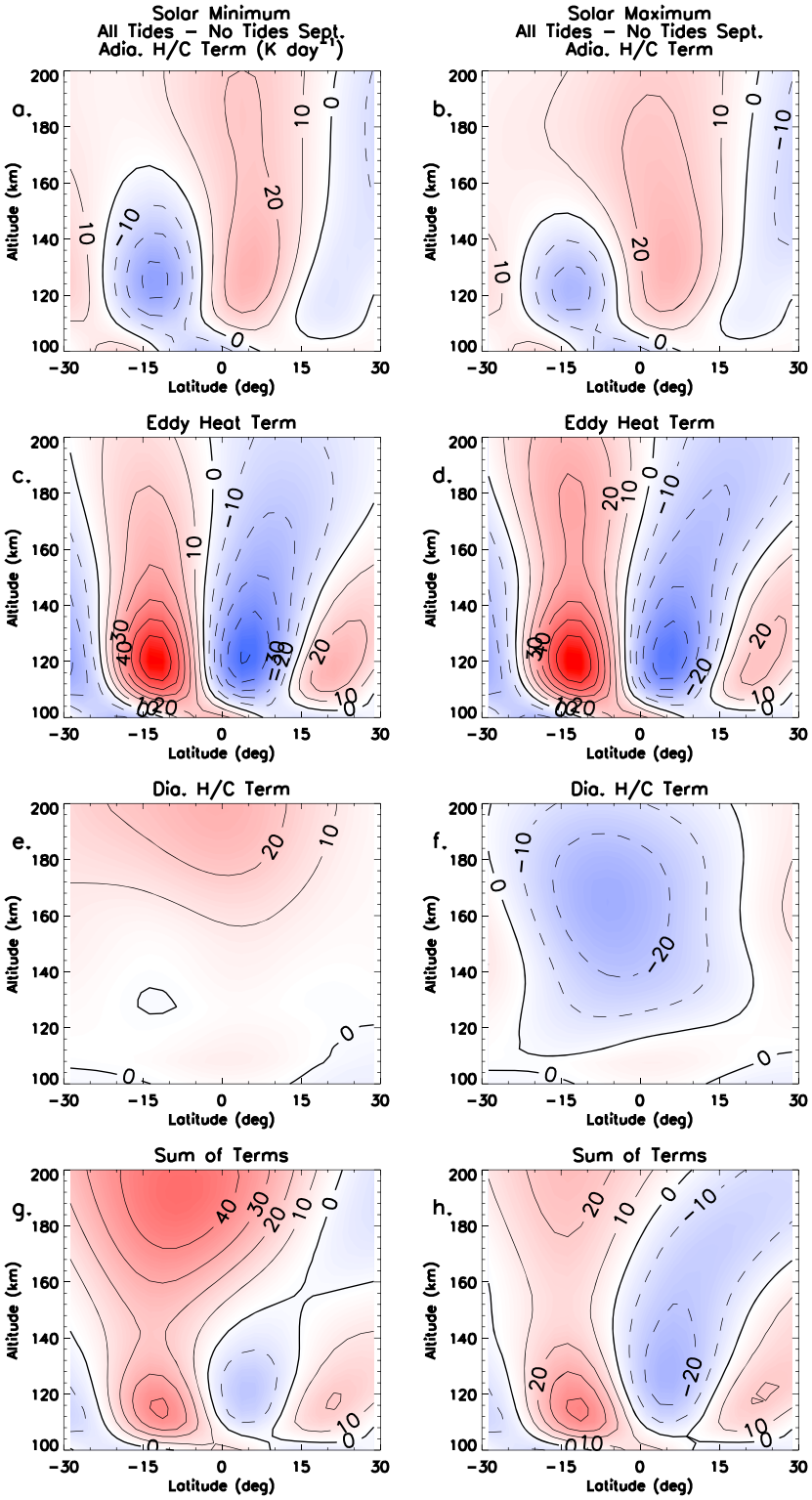

Figure 2. Zonal-mean difference fields from individual terms in the thermodynamic energy equation calculated from TIE-GCM simulations with/without TBCs including the Aida. (a and b) H/C term, (c and d) Eddy Heat term, (e and f) the Dia. H/C term, and (g and h) the sum of the aforementioned terms during the month of September at low latitudes and between 100 and 200 km under solar minimum (Figures 2a, 2c, 2e, and 2g) and maximum (Figures 2b, 2d, 2f, and 2h) conditions. Zonal-mean forcing term differences are contoured every ±10 K d^{-1}.

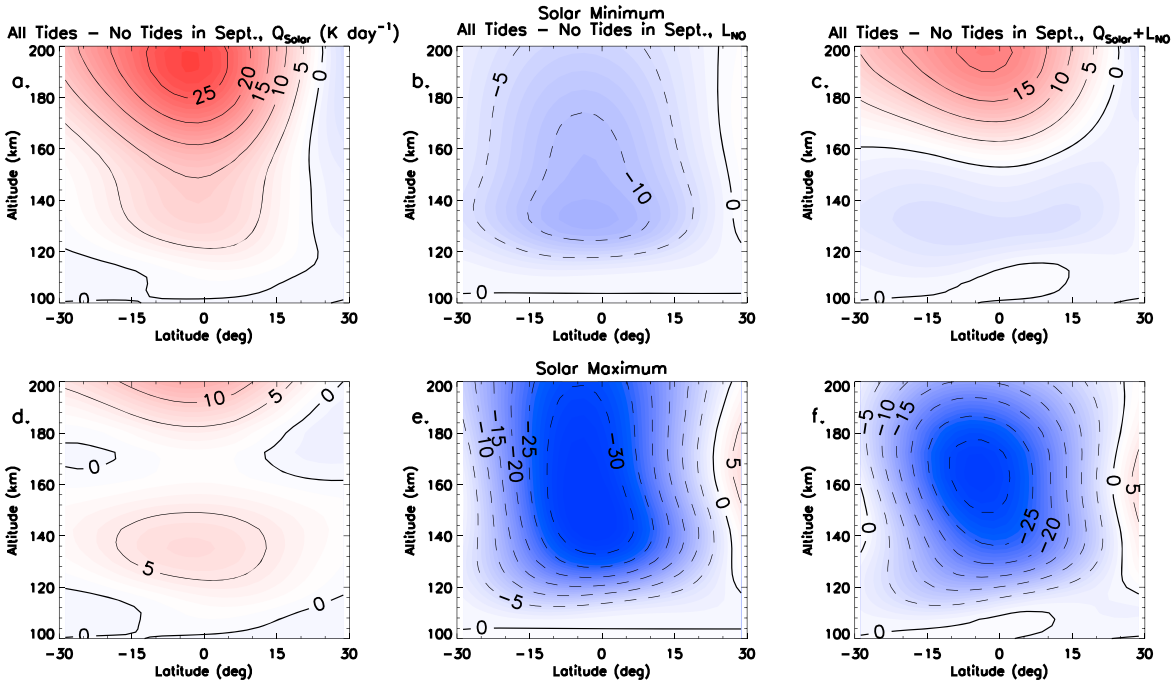

Figure 3. Zonal-mean diabatic heating and cooling term differences in the thermodynamic energy equation computed from TIE-GCM simulations with/without TBCs including the (a and d) radiative heating term (Q_{Solar}), (b and e) loss due to NO cooling (L_{NO}), and (c and f) the sum of differences during the month of September at low latitudes and between 100 and 200 km under solar minimum (Figures 3a–3c) and maximum (Figures 3d–3f) conditions. Zonal-mean forcing term differences are contoured every ±5 K d^{-1}.

and minima) of those differences shown for the Adia. H/C term, with values ranging from −50 to +60 K d^{-1}. Also, the tidal-induced changes in both the Adia. H/C and Eddy Heat terms do not exhibit noticeable solar cycle variations that would lead to changes in the zonal-mean temperature differences depicted in Figures 1a and 1c. Therefore, we deduce that neither tidal-induced adiabatic heating and cooling (and thus the zonal-mean residual circulation induced by tides) nor direct tidal heat transport is responsible for driving the solar cycle variability associated with the zonal-mean temperature differences in our TIE-GCM simulations.

Figures 2e and 2f clearly show that tidally driven Dia. H/C term differences exhibit strong solar cycle variations with mainly positive differences occurring at solar minimum and negative differences at solar maximum. Under solar minimum (maximum) conditions Dia. H/C differences are relatively small at low latitudes below ~150 km (~120 km), while above ~150 km (~120 km) differences increase (decrease) up (down) to +25 K d^{-1} (−25 K d^{-1}) in Figure 2e (Figure 2f). The solar cycle variability associated with the changes in Dia. H/C are in the same sense as that of the zonal-mean temperature differences shown in Figures 1a and 1c, which depict increases in the zonal-mean temperature at solar minimum and decreases in the zonal-mean temperature at solar maximum. This same type of solar cycle variability also manifests itself in the sum of the Adia. H/C, Eddy Heat, and Dia. H/C term differences at solar minimum and maximum (Figures 2g and 2h). Similarities in latitudinal and altitudinal structure between Figures 2c–2d and Figures 2g–2h show that the Eddy Heat term is primarily responsible altering the zonal-mean temperature distribution in the thermosphere. However, solar cycle variations in the Dia. H/C term lead to solar cycle variability in the tidal-induced zonal-mean temperature differences in the TIE-GCM. Evidence for the previous claim is provided by comparing Figures 2g and 2h. Specifically, the −10 K d^{-1} decrease calculated near the equator and 120 km in Figure 2g at solar minimum reaches values of −25 K d^{-1} at solar maximum that extend to higher latitudes and altitudes in Figure 2h. Also, the +45 K d^{-1} increase above 180 km depicted in Figure 2g at solar minimum is reduced to +20 K d^{-1} at solar maximum and its latitudinal extent is more confined in Figure 2h. The upshot of the above discussion is that solar cycle variability in the zonal-mean thermal balance of IT system is induced by the tides through the Dia. H/C term in the zonal-mean thermodynamic energy equation.

As previously stated the diabatic heating and cooling term in the TIE-GCM is determined by the differences between heating source terms and chemical cooling terms. Figure 3 shows the changes in the radiative

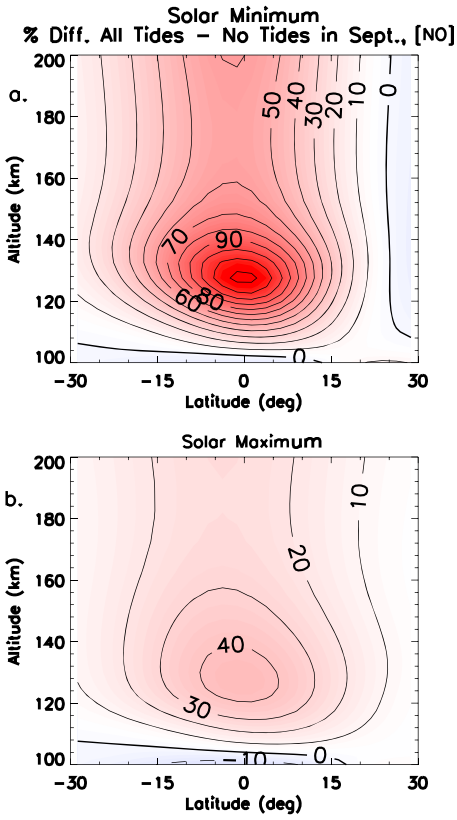

Figure 4. Percent changes in [NO] from TIE-GCM simulations with/without TBCs at low latitudes (±30°) and between 100 and 200 km during September under (a) solar minimum and (b) maximum conditions. Percent differences are contoured every ±10%.

heating (Q_{Solar}), NO cooling (L_{NO}), and the sum of these two due the tides under solar minimum and solar maximum conditions during the month of September. Only the tidal-induced changes in Q_{Solar} and L_{NO} are shown in Figure 3 because the sum of these differences depicted in Figures 3c and 3f account for most of the full Dia. H/C term differences shown in Figures 2g and 2h. Comparing the differences in Figures 3a–3c and Figures 3d–3f makes it easy to see that the solar cycle variability in the zonal-mean temperature differences driven by the tides results from changes in the NO cooling via the Dia. H/C term in the zonal-mean thermodynamic energy equation. Stronger (weaker) positive differences between TIE-GCM simulations with/without TBCs are on the order of +25 K d^{-1} (+10 K d^{-1}) in the radiative heating are reduced by weaker (stronger) negative differences in NO cooling of −10 K d^{-1} (−30 K d^{-1}) in the lower thermosphere. The aggregate of effect of increased NO cooling during solar maximum is shown in Figure 3f and leads to a 25 to 30 K d^{-1} net reduction in the Dia. H/C term. This ∼30 K d^{-1} decrease in the Dia. H/C term is at least 25 K d^{-1} stronger than aggregate differences in the radiative heating and NO cooling illustrated in Figure 3c during solar minimum. Therefore, the +19 K zonal-mean temperature differences at low-latitudes driven by the Adia. H/C, Eddy Heat, and Dia. H/C during solar minimum (Figure 1a) are reduced by the intensified NO cooling forced by the dissipating tides to −8 K during solar maximum (Figure 1c). In the subsequent subsection we investigate how the tides act to change the NO IR cooling in the TIE-GCM.

3.3. Tidal-Induced NO Variations at Solar Minimum and Maximum

NO and the 5.3 μm emission from NO are important to the aeronomy and thermal balance of the IT system and are known to vary substantially with solar [e.g., *Mlynczak et al.*, 2010, 2014] and auroral activity [e.g., *Solomon et al.*, 1999; *Barth et al.*, 2003; *Knipp et al.*, 2013]. As stated in section 1 and illustrated in section 3.2, the dissipating tides augment the NO 5.3 μm IR cooling in the lower thermosphere, and these changes depend on longitude, latitude, altitude, and solar cycle. Therefore, this subsection focuses on investigating the mechanism by which the vertically propagating tides are acting to enhance NO cooling in the lower IT, with specific attention to the solar cycle variations associated with this mechanism.

Mlynczak et al. [2003] listed a number of different processes that can lead to changes in the amount of radiation emitted by NO including the following: (1) increased NO number density ([NO]); (2) increased temperature; (3) exothermic production of NO; and (4) increased O number density ([O]). For example, process (3) occurs during increased geomagnetic activity and thus is not important in our numerical experiments because the geomagnetic proxies are set and held constant at values representative of quiescent conditions. Outside of the inherent temperature increase with solar cycle, the effect of process (2) on our TIE-GCM results is comparatively small, as changes in the zonal-mean temperature induced by tidal dissipation only vary by at most ±20 K (see Figures 1a–1c). Thus, processes (1) and (4) are most likely producing the solar cycle variability in the Dia. H/C term and the zonal-mean temperature differences depicted in Figures 1–3.

The effect of increased [NO] on the Dia. H/C term in the zonal-mean thermodynamic energy equation due to the dissipating tides is quantified in Figure 4, which shows the percent changes in [NO] between TIE-GCM simulations with/without TBCs under solar minimum (Figure 4a) and maximum (Figure 4b) conditions in the

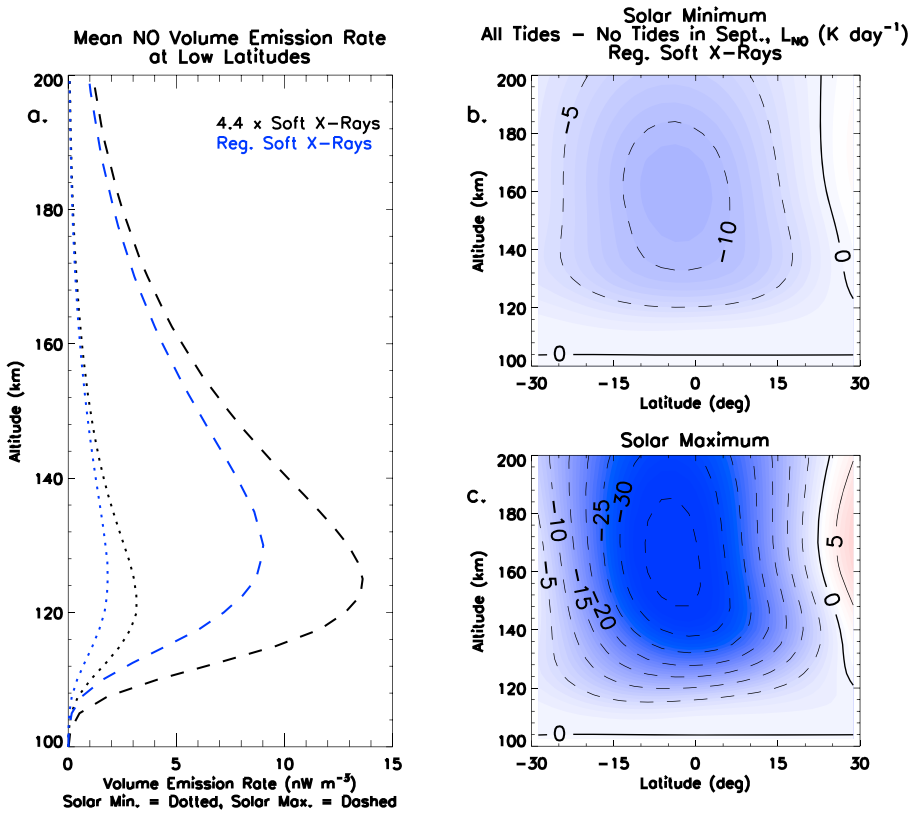

Figure 5. (a) Zonal-mean NO volume emission rate (VER) averaged over low latitudes (±30°) and between 100 and 200 km during September under solar minimum (dotted lines) and maximum (dashed lines) conditions. Black (Blue) lines represent TIE-GCM simulations performed using higher (baseline) soft X-ray solar fluxes. (b and c) Same as Figures 3b and 3e, respectively, except from TIE-GCM simulations performed using the baseline soft X-ray solar fluxes.

lower thermosphere. At solar minimum (maximum) tidal dissipation increases the [NO] by up to 120% (40%) between 100 and 200 km at low latitudes, with the largest changes centered over the equator. These large increases and their latitude-altitude extent are consistent with more NO cooling due to the tides at solar minimum and maximum, and low latitudes up to ~200 km in Figures 3b and 3e, respectively. Although the tides have a greater impact on the [NO] at solar minimum (i.e., larger relative increase in [NO]), their influence on the 5.3 μm NO cooling is largest at solar maximum when the NO volume emission rates (VER and thus [NO]) are a factor of ~4 higher than at solar minimum (Figure 5). In this way the tides act to additionally enhance the inherent solar cycle behavior of [NO] in the lower thermosphere. While the largest changes in [NO] in Figure 4 and the diabatic heating and cooling terms in Figure 3 are located over the equator, greater changes in the zonal-mean temperatures due to the tides in Figures 1a–1c do occur (e.g., the <−10 K in Figure 1c above ±15° latitude) as a result of the residual meridional circulation driven by the tides, which leads to upwelling at low to middle latitudes (i.e., analogous to the type described by *Yamazaki and Richmond* [2013] for the DW1).

Before proceeding further in our analysis of the tidal mechanisms responsible for driving [NO] changes in the equatorial lower thermosphere, we return to the question raised in section 2, as to the sensitivity of NO and its 5.3 μm emission to increased solar soft X-ray fluxes. To further explore this possibility, consider Figure 5, which displays how changes in the solar soft X-ray fluxes impact the NO cooling in the equatorial lower thermosphere in the TIE-GCM. Specifically, Figure 5a depicts the mean NO VER under solar minimum (dotted lines) and maximum (dashed lines) conditions for the increased (black lines) [after *Fang et al.*, 2008] and baseline (blue lines) soft X-rays. Analogous to what was reported by *Siskind et al.* [1990], increasing the solar soft X-rays increases NO VERs as a result of increased [NO]. The NO VER at solar minimum forced with the baseline solar soft X-rays in the TIE-GCM is comparable to thermosphere-ionosphere-mesosphere-electrodynamics general

circulation model (TIME-GCM) results presented in *Oberheide et al.* [2013]. However, the NO VER illustrated in Figure 5a (and in *Oberheide et al.* [2013]) at solar minimum and maximum is at least a factor 2 higher than those measured by the Michelson Interferometer for Passive Atmospheric Sounding (MIPAS) [after *Oberheide et al.*, 2013] and SABER [*Mlynczak et al.*, 2010; *Oberheide et al.*, 2013]. Thus, increasing the solar soft X-rays in the TIE-GCM only further increases the discrepancies between modeled (i.e., TIE-GCM and TIME-GCM) and measured NO VERs. Conversely, a comparison between Figures 5b and 5c and Figures 3b and 3e shows that the tidal-induced changes in the NO cooling at solar minimum and maximum are unaffected by changes in the solar soft X-ray flux (i.e., differences of only -2 K d^{-1}). This is also the case for the tidal-induced zonal-mean temperature and constituent differences (i.e., only varying by $\pm 2-3$ K and 5–10%); therefore, increases in TIE-GCM solar soft X-ray fluxes have little consequence for the subsequent analysis of the different tidal mechanisms responsible for altering the NO cooling in the equatorial lower thermosphere, as well as on the results and conclusions presented herein. It should also be emphasized that performing a "cost-benefit" analysis of the trade-offs between improved TIE-GCM electrodynamics and improved TIE-GCM *E* region neutral chemistry via solar soft X-ray changes is outside the scope of this paper but does warrant additional analysis.

In order to understand how the tides are acting to change the [NO], one must analyze the [NO] continuity equation. Following the methodology and terminology described above for deriving the zonal-mean thermodynamic energy equation and *Jones et al.* [2014b] for the zonal-mean [O] continuity equation, we arrive at the zonal-mean [NO] continuity equation including production and loss:

$$\frac{\partial \overline{[\mathrm{NO}]}}{\partial t} = \overline{P} - \overline{L[\mathrm{NO}]} - \frac{\partial}{\partial \theta}\overline{v}\,\overline{[\mathrm{NO}]} - \frac{\partial}{\partial z}\overline{w}\,\overline{[\mathrm{NO}]} - \frac{\partial}{\partial \theta}\overline{v'[\mathrm{NO}]'} - \frac{\partial}{\partial z}\overline{w'[\mathrm{NO}]'}, \tag{2}$$

where P (L) is the production (loss) of [NO]. Below, we outline the main (i.e., a first-order set of reactions) production and loss mechanisms of [NO] in the TIE-GCM [after *Roble and Ridley*, 1987; *Roble et al.*, 1987; *Roble*, 1995]. Close to the TIE-GCM lower boundary (below ~110 km) production of [NO] mainly occurs via

$$\mathrm{N}(^2\mathrm{D}) + \mathrm{O}_2 \rightarrow \mathrm{NO} + \mathrm{O}. \tag{R1}$$

Above ~110 km the following temperature-dependent reaction becomes the dominant source of NO:

$$\mathrm{N}(^4\mathrm{S}) + \mathrm{O}_2 \rightarrow \mathrm{NO} + \mathrm{O}. \tag{R2}$$

In the lower thermosphere the principal loss mechanism for NO is with ground state atomic nitrogen (N(^{4}S)):

$$\mathrm{NO} + \mathrm{N}(^4\mathrm{S}) \rightarrow \mathrm{N}_2 + \mathrm{O}. \tag{R3}$$

Lastly, a much smaller and less important loss mechanism for NO is with excited atomic nitrogen (N(^{2}D)):

$$\mathrm{NO} + \mathrm{N}(^2\mathrm{D}) \rightarrow \mathrm{N}(^4\mathrm{S}) + \mathrm{O}. \tag{R4}$$

The reaction rates for (R1)–(R4) are $\beta_1 = 5 \times 10^{-12}$ cm^3 s^{-1}, $\beta_2 = 1.510 \times 10^{-11} \exp(\frac{-3600}{T})$ cm^3 s^{-1}, $\beta_3 = 3.410 \times 10^{-11}\sqrt{\frac{T}{300}}$ cm^3 s^{-1}, and $\beta_4 = 7 \times 10^{-11}$ cm^3 s^{-1} [after *Roble and Ridley*, 1987; *Roble et al.*, 1987; *Roble*, 1995]. The third and fourth terms on the right-hand side of equation (2) represent meridional and vertical advective tidal transport of [NO] (i.e., the transport of [NO] due to tidally induced zonal-mean winds) or the mechanism described by *Yamazaki and Richmond* [2013]. The last two terms on the right-hand side of equation (2) represent meridional and vertical net tidal transport of [NO] (i.e., [NO] transport due to the tides themselves via [NO] flux divergence) or the mechanism described in *Jones et al.* [2014b].

The largest [NO] differences displayed in Figure 4 occur in the altitude regime where transport, chemical, and diffusion processes could be of equal importance. To determine which one of the above processes is of utmost

importance in the lower thermosphere, one can refer to their respective time constants, which are calculated using the following:

$$\tau_{\mathrm{chem_{NO}}} = \frac{1}{\beta_3\overline{[\mathrm{N}(^4\mathrm{S})]} + \beta_4\overline{[\mathrm{N}(^2\mathrm{D})]}},$$

$$\tau_{\mathrm{eddy}} = \frac{\overline{H}^2}{\overline{K_{zz}}},$$

$$\tau_{\mathrm{mole}} = \frac{\overline{H}^2_{\mathrm{NO}}}{\overline{D(\mathrm{NO}, \mathrm{N}_2)}},$$

$$\tau_{v,\mathrm{trans}} = \frac{L}{v_{\mathrm{Tidal}}},$$

$$\tau_{w,\mathrm{trans}} = \frac{\overline{H}_{\mathrm{NO}}}{w_{\mathrm{Tidal}}},$$

$$\tau_{v,\mathrm{adv}} = \frac{L}{v_{\mathrm{adv}}},$$

$$\tau_{w,\mathrm{adv}} = \frac{\overline{H}_{\mathrm{NO}}}{w_{\mathrm{adv}}},$$

where K_{zz} is the eddy diffusion coefficient from the TIE-GCM, H_{NO} is the diffusive-equilibrium scale height of NO, $\mathrm{D}(\mathrm{NO}, \mathrm{N}_2)$ is the mutual diffusion coefficient [after *Banks and Kockarts*, 1973], L is the characteristic meridional length (we assumed it to be $\sim 10^\circ$ in latitude or 1000 km), v_{Tidal} (w_{Tidal}) is the *effective* meridional (vertical) net *tidal* transport velocity that is defined as $\overline{v'[\mathrm{NO}]'} \approx v_{\mathrm{Tidal}}\overline{[\mathrm{NO}]}$ ($\overline{w'[\mathrm{NO}]'} \approx w_{\mathrm{Tidal}}\overline{[\mathrm{NO}]}$) [after *Gardner and Liu*, 2010], and v_{adv} (w_{adv}) is equal to $\overline{v}$ ($\overline{w}$) or the zonal-mean meridional (vertical) wind. Figure 6 shows the time constants for the terms in the NO continuity equation as a function of altitude and solar cycle averaged over low latitudes in the lower thermosphere. Down close to the TIE-GCM lower boundary (~100 km) the lifetime of NO due to tidal and advective (in both directions) transport, as well as eddy and molecular diffusion, are on the order of 10 days at all levels of solar activity (Figure 6). However, at altitudes where the [NO] changes are largest due to the tides in Figures 4a and 4b the chemical time constant (black lines, Figure 6) is shorter than all other time constants, including molecular diffusion (cyan lines, Figure 6) at all levels of solar activity. Specifically, the chemical lifetime of NO is shorter than a day starting at ~125 km (~145 km) under solar minimum (maximum) conditions in the TIE-GCM, suggesting that NO is not in diffusive equilibrium. This means that the dynamical effects of the tides on the NO distribution are playing a comparatively small role in determining the zonal-mean NO distribution in the thermosphere, unlike that of O [see *Yamazaki and Richmond*, 2013; *Jones et al.*, 2014b]. Therefore, it must be through the production and loss terms in the zonal-mean [NO] continuity equation that the tides are acting to change the [NO] and thus the NO 5.3 μm IR cooling in the TIE-GCM.

To further elucidate how the tides modulate the production and loss terms in the [NO] continuity equation, ultimately driving the percent changes in [NO] shown in Figure 4, we assumed that [NO] was in chemical equilibrium and derived a simplified equation using chemical reactions (R1)–(R4) following *Siskind et al.* [2004]:

$$\overline{[\mathrm{NO}]}_{\mathrm{chem}} = \frac{\left(\overline{\beta_1}\overline{[\mathrm{N}(^2\mathrm{D})]} + \overline{\beta_2}\overline{[\mathrm{N}(^4\mathrm{S})]}\right)\overline{[\mathrm{O}_2]}}{\overline{\beta_4}\overline{[\mathrm{N}(^2\mathrm{D})]} + \overline{\beta_3}\overline{[\mathrm{N}(^4\mathrm{S})]}} \approx \overline{[\mathrm{NO}]}, \tag{3}$$

where $[\mathrm{O}_2]$ is the molecular oxygen number density. Figures 7a and 7d illustrate the percent changes calculated assuming [NO] is in chemical equilibrium (i.e., $[\mathrm{NO}]_{\mathrm{Chem}}$) from equation (3) between TIE-GCM with/without TBCs at solar minimum and maximum in lower equatorial thermosphere. Figures 7a and 7d

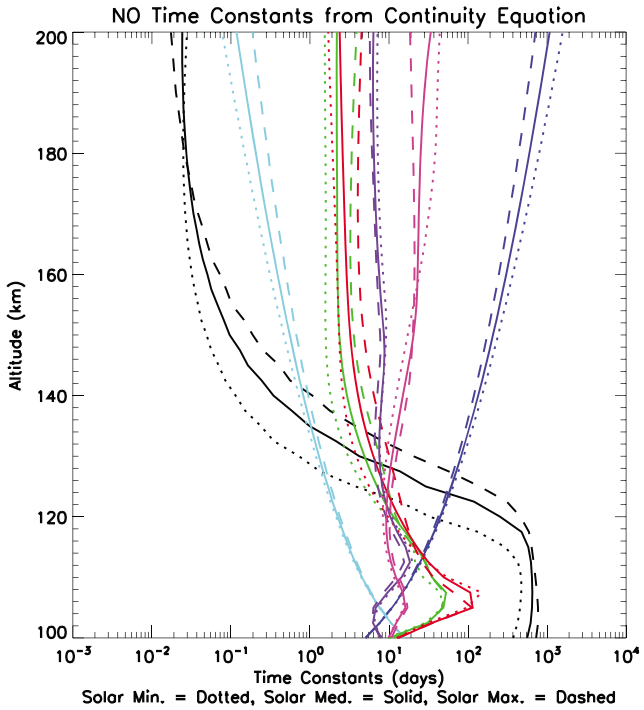

Figure 6. NO time constants averaged over low latitudes (±30°) for chemistry (black), eddy diffusion (blue), molecular diffusion (cyan), tidal transport (green and red), and advective transport (purple and magenta) as a function of altitude during September under solar minimum (dotted), medium (solid), and maximum (dashed) conditions.

reveal that the zonal-mean NO distribution in the equatorial lower thermosphere is mainly in chemical equilibrium, as percent changes in $[NO]_{Chem}$ can almost replicate the differences calculated not assuming NO is in chemical equilibrium (Figures 4a and 4b). In particular, the latitudinal and vertical structure of $[NO]_{Chem}$ differences display maxima of ~135% (~50%) at ~125 km consistent with those depicted in Figure 4a (Figure 4b) during solar minimum (maximum), which then extend above 200 km with values on the order of ~60% (~30%). With that being said, the $[NO]_{Chem}$ maxima during solar minimum and maximum are larger by about 10–15% of those calculated for [NO], which quantifies the role the other mechanisms, including dynamics and diffusion play in changing the [NO] as a result of tidal dissipation.

The remaining four plots in Figure 7 show that the main way the tides act to alter the NO chemistry is through $[O_2]$, leading to increased production in reactions (R1) and (R2), which is also reflected by a decrease in $[N(^4S)]$ (and $[N(^2D)]$, not shown). Figures 7b and 7e (Figures 7c and 7f) illustrate mostly increases (decreases) in $[O_2]$ ($[N(^4S)]$) in the equatorial lower thermosphere with differences of at least +15% (−30%) occurring at the altitudes where the [NO] percent changes reach their maximum when the tides are included at the TIE-GCM lower boundary. In addition, Figure 7 shows that the tides have a larger impact on the $[O_2]$ and $[N(^4S)]$ during solar minimum as compared to solar maximum, offering an explanation as to why the increase in [NO] is larger at solar minimum.

The above explanation for the more pronounced increase of [NO] at solar minimum as compared to solar maximum is further strengthened by the results depicted in Figure 8. Specifically, Figure 8a shows that the O/O_2 ratio is decreased more under solar minimum conditions (dotted line) than under solar maximum conditions (dashed line) in the equatorial lower thermosphere, with values ranging from −22 to −16% and from −18 to −13%, respectively. *Siskind et al.* [1989] showed that [NO] is inversely proportional to the O/O_2 ratio, so a greater reduction in the O/O_2 ratio at solar minimum versus that calculated at solar maximum leads to larger [NO] percent changes attributable to the tides at solar minimum in the TIE-GCM. Figures 8c and 8e depict this inverse relationship in a latitude-height representation of Figure 8a and clearly illustrate that the larger reduction in O/O_2 (<−30%) centered over the equator leads to a larger increase in [NO] in Figures 4a and 7a at solar minimum as compared to solar maximum. Greater reductions in the O/O_2 ratio driven by the dissipating tides result from larger increases in $[O_2]$ (Figure 7b) and larger decreases in [O] (Figure 8b) at solar minimum as

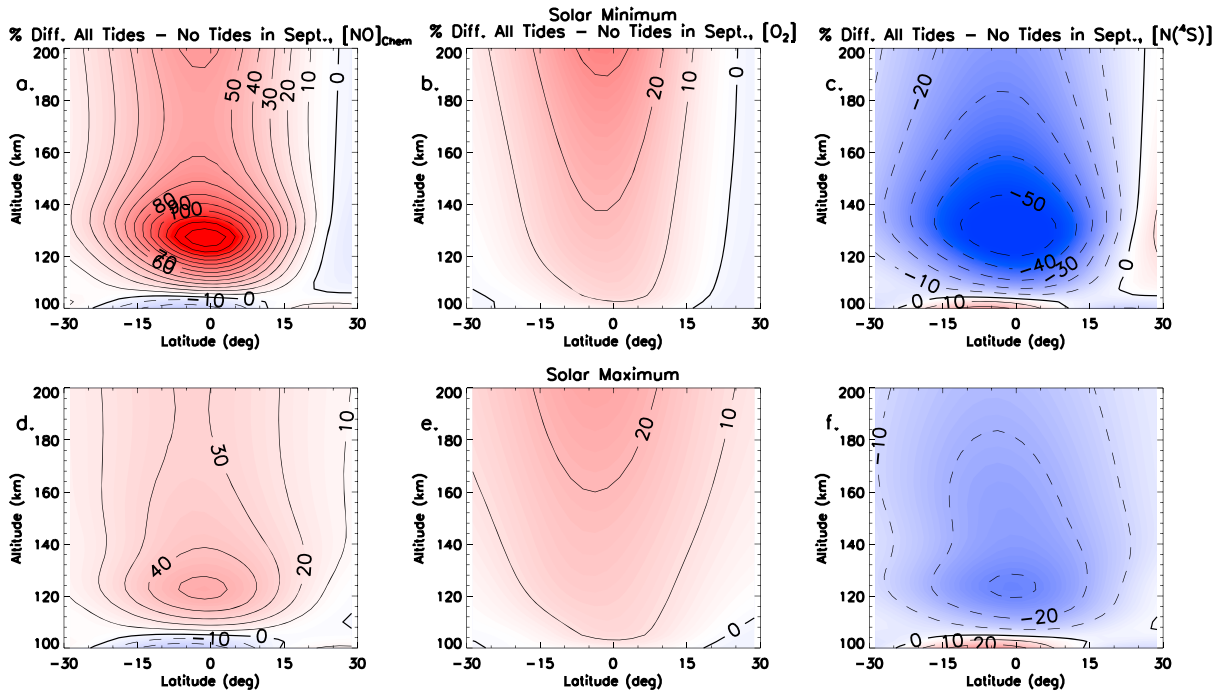

Figure 7. Percent changes in (a and d) $[NO]_{Chem}$, (b and e) $[O_2]$, and (c and f) $[N(^4S)]$ from TIE-GCM simulations with/without TBCs at low latitudes and between 100 and 200 km during September under solar minimum (Figures 7a–7c) and maximum (Figures 7d–7f) conditions. Percent differences are contoured every ±10%.

compared to solar maximum (Figures 7e and 8d). Also, not only is there more O generated naturally to collide with NO causing spontaneous emission of IR radiation at solar maximum than at solar minimum; the reduction in [O] due to the tides is smaller at solar maximum than at solar minimum (in a relative sense not in an absolute sense, Figures 8b and 8d), thereby leading to more tidal-induced NO cooling at solar maximum than at solar minimum. Therefore, we can conclude that tidal-induced changes in the major neutral constituents of the thermosphere act to modulate the thermosphere's "natural thermostat" or NO 5.3 μm IR cooling [*Mlynczak et al.*, 2003], thereby generating solar cycle variability in the zonal-mean thermal energy budget via diabatic heating and cooling.

We diagnose tidal-induced changes in $[O_2]$ by deriving time constants for transport, chemical, and diffusion processes that describe the lifetime of a O_2 molecule in the lower thermosphere. The time constants for eddy diffusion and meridional transport of O_2 (both advective and tidal) are the same as those shown above for NO, except that $\overline{v'[O_2]'} \approx v_{\text{Tidal}}\overline{[O_2]}$. The time constants for chemistry, molecular diffusion, and vertical transport of O_2 (both advective and tidal) have changed slightly from their form above to include the loss of O_2 due to $N(^2D)$ and $N(^4S)$, as well as charge exchange with O^+, the mutual diffusion coefficient of O_2 ($D(O_2, N_2)$) [after *Colegrove et al.*, 1966], the diffusive-equilibrium scale height of O_2 (H_{O_2}), and w_{Tidal} now accounts for O_2 ($\overline{w'[O_2]'} \approx w_{\text{Tidal}}\overline{[O_2]}$) resulting in the following:

$$\tau_{\text{chem}_{O_2}} = \frac{1}{\beta_1\overline{[N(^2D)]} + \beta_2\overline{[N(^4S)]} + k_1\overline{[O^+]}},$$

$$\tau_{\text{mole}} = \frac{\overline{H}^2_{O_2}}{\overline{D(O_2, N_2)}},$$

$$\tau_{w,\text{trans}} = \frac{\overline{H}_{O_2}}{w_{\text{Tidal}}},$$

$$\tau_{w,\text{adv}} = \frac{\overline{H}_{O_2}}{w_{\text{adv}}},$$

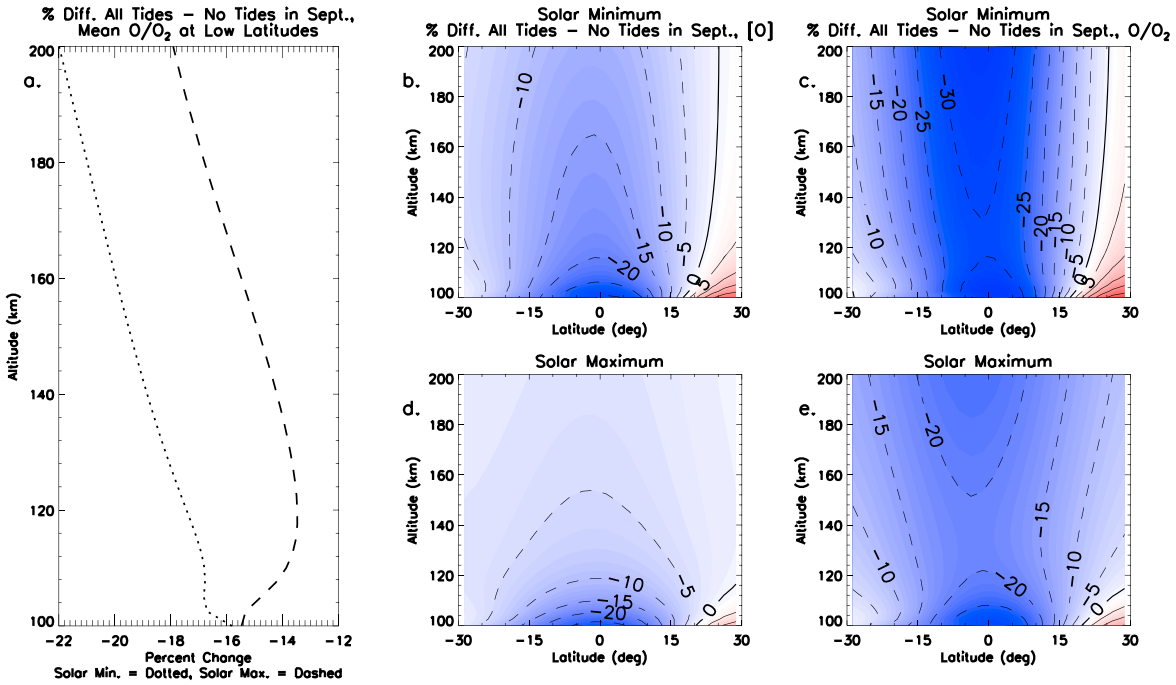

Figure 8. (a) Percent changes in zonal-mean O/O_2 ratio averaged over low latitudes from TIE-GCM simulations including CTMT lower boundary tidal forcing between 100 and 200 km during September under solar minimum (dotted line) and maximum (dashed line) conditions. (b–e) Percent changes in [O] (O/O_2) from TIE-GCM simulations with/without TBCs at low latitudes and between 100 and 200 km during September. Differences computed from simulations under solar minimum (maximum) conditions are shown in Figures 8b and 8c (Figures 8d and 8e). Percent differences are contoured every ±5%.

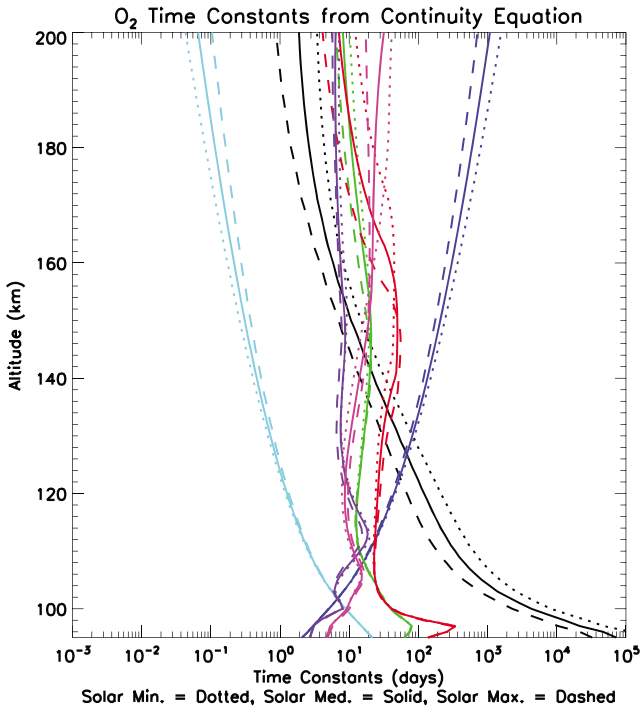

Figure 9. Same as Figure 6, except for O_2 time constants that extend down to the TIE-GCM lower boundary of 97 km.

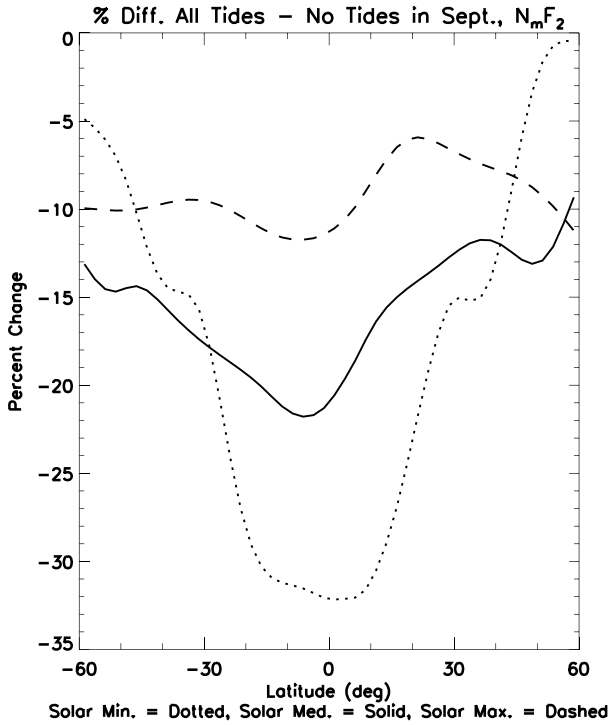

Figure 10. Percent changes in N_mF_2 between TIE-GCM simulations with/without TBCs at low and middle latitudes during September under solar minimum (dotted line), medium (solid line), and maximum (dashed line) conditions.

where $k_1 = 1.6\times10^{-11}\ T_1^{-0.52}+5.5\times10^{-11}\ \exp^{\left(\frac{-22.85}{T_1}\right)}$ [after *Roble et al.*, 1987], $T_1 = \frac{1}{300}\left(\frac{2}{3}T_i + \frac{1}{3}T\right)$, and T_i is the ion temperature. Figure 9 is the same as Figure 6, except for O_2 time constants. The lifetime of O_2 due to meridional and vertical advective (net tidal) transport ranges from ~1 to 10 days (~50 to 100 days) between 97 and 110 km close to the TIE-GCM lower boundary and these remain relatively constant with altitude (magenta, purple, green, and red lines in Figure 9). Due to the long lifetime of O_2 due to net tidal transport, compared to the tidal period (hours) and the time scales of diffusion and advective transport (~10 days below 105 km in Figure 9), the aforementioned *Jones et al.* [2014b] mechanism is not likely to generate the [O_2] changes illustrated in Figures 7b and 7e. Instead, it appears that advective transport time scales (magenta and purple lines in Figure 9) are short and comparable to those of eddy and molecular diffusion (blue and cyan lines in Figure 9), leading us to conclude that it is most likely advective tidal transport that is responsible for increasing the [O_2] in the TIE-GCM at all levels of solar activity. Specifically, this dynamically driven [O_2] increase via advective tidal transport is consistent with the [O] changes shown in Figures 8b and 8d and described in *Jones et al.* [2014b] (i.e., more [O_2] being forced vertically to be photodissociated in order to replenish the tidal-induced loss of [O]).

Although the solar cycle variability associated with tidal-induced changes in [NO], and thus NO cooling described above, can be explained by the solar cycle variability in tidal-induced [O] and [O_2] changes, it is less apparent what is driving the solar cycle variability associated with the tidal-induced [O] and [O_2] changes themselves. These solar cycle variations could be related to the products of tidal (primed) quantities in the [O] and [O_2] continuity equations (i.e., analogous to the last two terms in equation (2) and discussed in *Jones et al.* [2014b]), which would involve both in situ and upward propagating tides, the former varying with solar cycle. However, preliminary analysis of the dynamical term difference fields in the [O] and [O_2] continuity equations do not vary with solar cycle. This supports the findings of *Yamazaki and Richmond* [2013], which state that the in situ tides have little impact on the global mass mixing ratio of the major species in the thermosphere. Since tidal effects on the major species of the thermosphere are qualitatively consistent with increases in eddy diffusion, the individual species mass diverges away from the mean molecular weight more rapidly in altitude at solar maximum than in solar minimum, partially explaining greater [O_2] relative differences at solar minimum [see *Colegrove et al.*, 1965; *Nguyen and Palo*, 2014]. Another explanation for the solar cycle variations in tidal-induced [O] and [O_2] changes could be analogous to the solar cycle variations associated with the

relative density response to a geomagnetic storm at a fixed altitude; i.e., a higher relative density perturbation due to geomagnetic forcing occurs at solar minimum as compared to solar maximum due to more density scale height increments being integrated below a given altitude [see *Lei et al.*, 2010, 2011; *Prölss*, 2011]. We suspect that changes in the density scale heights of O and O_2 may only be partially responsible for the tidal-induced changes in [O_2] and [O] depicted in Figures 7 and 8. These different processes briefly outlined above, and potentially others that produce solar cycle variations in tidal-induced change in [O] and [O_2], merit further investigation.

3.4. Implications for Tidal-Induced Solar Variability in the Ionosphere

A likely consequence of solar cycle variability in the zonal-mean thermal energy budget through tidal-induced neutral composition changes is solar cycle variability in the ionosphere. Specifically, *Jones et al.* [2014a] [*Siskind et al.*, 2014] showed that up to a ~20% decrease in the electron density at the F_2 layer pear (N_mF_2) was driven by decreases in [O] and increases in [O_2] due to the tides at solar medium (minimum) in their TIE-GCM simulations. Figure 10 shows that there is solar cycle variability not only in the zonal-mean temperatures but also in the N_mF_2 driven by the dissipating tides through major neutral constituent changes. Decreases of ~32%, ~22%, and ~12% in N_mF_2 arise from percent decreases in [O] (source) and percent increases in [N_2] and [O_2] (loss) at solar minimum (dotted line), medium (solid line), and maximum (dashed line), respectively, during September in the equatorial ionosphere. Larger reductions of electron density during solar minimum as compared to solar maximum are driven by greater [O] depletions and [O_2] enhancements at solar minimum versus that of solar maximum (see Figures 7 and 8).

4. Summary and Conclusion

The impacts that the vertically propagating tides have on the zonal-mean thermal energy budget and compositional structure of the IT system, as well as the underlying physical processes responsible for driving variability in the two have garnered little attention over the past half a century. Therefore, this paper investigates the role that atmospheric tides play in driving solar cycle variability of the zonal-mean temperature structure of the IT. The ways by which the dissipating tides act to change the zonal-mean temperatures of the IT are evaluated by calculating difference fields in the zonal-mean thermodynamic energy equation forcing terms and subsequently neutral constituent densities between TIE-GCM simulations with/without observationally based background and tidal lower boundary conditions. The primary results and conclusions to emerge from our numerical experiments are as follows:

1. Zonal-mean temperature differences calculated from the TIE-GCM are strongly dependent upon solar cycle. Maximum (minimum) zonal-mean temperature differences of up to +19 K (−15 K) occur under solar minimum (maximum) conditions during September in the equatorial IT. The zonal-mean temperature differences in the lower thermosphere can be almost completely explained due to dissipation of DW1 and SW2 (Figure 1). These tides have their largest effects on the zonal-mean temperature below 200 km, whereas above 200 km temperature differences remain relatively constant with altitude due to the increased importance of thermal conductivity.
2. Diagnosis of the individual terms in the thermodynamic energy equation reveals that the dissipating tides act to alter the zonal-mean temperature structure of the IT system through adiabatic heating and cooling, eddy heat source, and diabatic heating and cooling terms. Specifically, tidal dissipation induces the largest changes in the eddy heat flux divergence (e.g., −50 to +60 K d^{-1} in Figures 2c and 2d) at all levels of solar activity and thus is mainly responsible for altering the zonal-mean temperature distribution in the equatorial lower thermosphere. However, the direct heat transport due to the tides does not vary much with solar activity, whereas the relative importance of the diabatic heating and cooling term is strongly dependent upon solar cycle exhibiting +25 K d^{-1} values at solar minimum and −25 K d^{-1} at solar maximum (Figure 2). Ultimately, these tidal-induced changes in the diabatic heating and cooling terms lead to a 30 K change between zonal-mean temperature differences at low latitudes under solar minimum and maximum conditions (Figures 1a–1c).
3. Tidal dissipation alters the diabatic heating and cooling term in the thermodynamic energy equation through changes in solar radiation absorption and NO cooling in the TIE-GCM. Specifically, the tides strengthen the natural thermostat of the thermosphere [*Mlynczak et al.*, 2003] or NO 5.3 μm IR cooling by 10 K d^{-1} and 30 day^{-1} at solar minimum and maximum, respectively (Figures 3b and 3e). Essentially, constant tidal forcing at the TIE-GCM lower boundary modulates the intrinsic solar cycle behavior of the "natural

thermostat" of the thermosphere, which results in more (less) tidal-induced cooling at solar maximum (minimum). These tidal-induced changes in NO cooling and their associated solar cycle variability are insensitive to increased solar soft X-rays in the TIE-GCM. To further quantify this NO cooling enhancement due to the tides, typical zonal-mean NO cooling enhancements as a result of solar cycle range from ~100 to 200 K d^{-1} in the TIE-GCM, implying that the tides could act to modulate the NO cooling mechanism by some ~5–30% depending on solar cycle. Additionally, the vertical extent of the largest NO cooling differences induced by the tides depicted in Figure 3 can be affected by the in situ driven SW2; i.e., the SW2 forced by IR and UV radiation in the lower atmosphere combines with the SW2 forced in situ in the thermosphere to produce solar cycle variability in the vertical extent (and distribution) of NO cooling differences.

4. The solar cycle variations in the major neutral constituents (particularly in $[O_2]$) lead to 120% (40%) increases in [NO] (Figures 4a and 4b), mainly via the production and loss terms in the zonal-mean [NO] continuity equation (Figures 6, 7a, and 7d), ultimately resulting in increased NO or diabatic cooling in the zonal-mean thermosphere. Greater [NO] enhancements occur at solar minimum than at solar maximum due to greater enhancements (reductions) in $[O_2]$ (the O/O_2 ratio) in the TIE-GCM (e.g., see Figures 7b, 7e, and 8). Although [NO] enhancements are greater at solar minimum as compared to solar maximum, NO more efficiently cools the lower IT at solar maximum when the neutral densities of the thermosphere (especially in NO and O) are at their largest. In addition to tidal-induced solar cycle variability of [NO], *Jones et al.* [2014a] showed that there is seasonal variability associated with [O] and $[O_2]$ tidal-induced changes, suggesting that the tidally driven effects on [NO], and thus the zonal-mean thermospheric energy budget will vary intraannually as well.
5. Changes of +10% or greater in $[O_2]$ in the equatorial lower thermosphere are forced by advective tidal meridional and vertical transport of $[O_2]$ [after *Yamazaki and Richmond*, 2013] in a way that is in agreement with [O] depletions in the lower thermosphere. Time constants derived from the zonal-mean $[O_2]$ continuity equation show that the net tidal transport mechanism [after *Jones et al.*, 2014b] is not a primary driver of $[O_2]$ changes in the TIE-GCM at lower thermospheric altitudes.
6. Regardless of solar cycle there is a decrease in N_mF_2 when tides are included at the TIE-GCM lower boundary (Figure 10). N_mF_2 decreases at low and middle latitudes range from −32 to −5% throughout the solar cycle, which are driven by the dissipating tides through decreases in the plasma production (i.e., [O]) and increases in the loss of ionospheric plasma (i.e., $[O_2]$ and $[N_2]$).
7. TIE-GCM results analyzed herein suggest that tidal modifications to the zonal-mean thermal energy budget and neutral constituents modulate their natural 11 year solar cycle behavior. Therefore, tidal effects on long-term changes and trends in the mean state of the IT system warrant consideration [cf. *Laštovička*, 2013; *Emmert*, 2015], as changes in the atmospheric tidal spectrum coming from below (e.g., ozone forcing of SW2) could have noticeable effects on the long-term trends in IT densities and temperatures that depend on solar cycle. Similar speculations have recently been made by *Oliver et al.* [2013] with regards to gravity waves.

Acknowledgments
This work was supported by NASA through interagency agreement NNH13AV24I to the U.S. Naval Research Laboratory and the Chief of Naval Research. Additional support for this work is by the way of a Predoctoral Fellowship from The Ford Foundation, a Graduate Research Assistantship from the High Altitude Observatory, and the University of Colorado Glenn Murphy Endowed Chair. This work was conducted while McArthur Jones Jr. held a National Research Council's Research Associateship. The authors wish to acknowledge Stanley C. Solomon, John T. Emmert, and Douglas P. Drob for valuable discussions regarding NO chemistry in the lower thermosphere and the TIE-GCM. The authors also wish to thank David E. Siskind for his thoughtful review of our manuscript prior to submission and for providing insight into NO chemistry in the lower thermosphere. TIE-GCM outputs in NetCDF format are available upon request from M. Jones Jr. (mcarthur.jones.ctr@nrl.navy.mil). NCAR is sponsored by the National Science Foundation. Any opinions, findings, and conclusions or recommendations expressed in this material are those of the author(s) and do not necessarily reflect the views of the National Science Foundation.

References

Akmaev, R. A., and G. M. Shved (1980), Modelling of the composition of the lower thermosphere taking account of the dynamics with applications to tidal variations of the [OI] 5577 Å airglow, *J. Atmos. Terr. Phys.*, *42*(8), 705–716, doi:10.1016/0021-9169(80)90054-9.

Banks, P. M., and G. Kockarts (1973), Chapter 15—Effects of Diffusion in the Heterosphere, in *Aeronomy*, edited by P. M. Banks and G. Kockarts, pp. 32–63, Elsevier, Acad. Press., doi:10.1016/B978-0-12-077802-7.50007-5.

Barth, C. A., K. D. Mankoff, S. M. Bailey, and S. C. Solomon (2003), Global observations of nitric oxide in the thermosphere, *J. Geophys. Res.*, *108*(A1), 1027, doi:10.1029/2002JA009458.

Colegrove, F. D., W. B. Hanson, and F. S. Johnson (1965), Eddy diffusion and oxygen transport in the lower thermosphere, *J. Geophys. Res.*, *70*(19), 4931–4941, doi:10.1029/JZ070i019p04931.

Colegrove, F. D., F. S. Johnson, and W. B. Hanson (1966), Atmospheric composition in the lower thermosphere, *J. Geophys. Res.*, *71*(9), 2227–2236, doi:10.1029/JZ071i009p02227.

Dickinson, R., E. C. Ridley, and R. G. Roble (1981), A three-dimensional general circulation model of the thermosphere, *J. Geophys. Res.*, *86*(A3), 1499–1512, doi:10.1029/JA086iA03p01499.

Dickinson, R. E., E. C. Ridley, and R. G. Roble (1975), Meridional circulation in the thermosphere I. Equinox conditions, *J. Atmos. Sci.*, *32*, 1737–1754.

Dickinson, R. E., E. C. Ridley, and R. G. Roble (1984), Thermospheric general circulation with coupled dynamics and composition, *J. Atmos. Sci.*, *41*(2), 205–219, doi:10.1175/1520-0469(1984)041<0205:TGCWCD>2.0.CO;2.

Emmert, J. T. (2015), Thermospheric mass density: A review, *Adv. Space Res.*, *56*(5), 773–824, doi:10.1016/j.asr.2015.05.038.

Evans, D. S. (1987), Global statistical patterns of auroral phenomena, in *Proceedings of the Symposium on Quantitative Modeling of Magnetospheric-Ionospheric Coupling Processes*, edited by Y. Kamide and R. A. Wolf, pp. 325–330, Kyoto Sangyo Univ., Kyoto, Japan.

Fang, T. W., A. D. Richmond, J. Y. Liu, A. Maute, C. H. Lin, C. H. Chen, and B. Harper (2008), Model simulation of the equatorial electrojet in the Peruvian and Philippine sectors, *J. Atmos. Sol. Terr. Phys.*, *70*(17), 2203–2211, doi:10.1016/j.jastp.2008.04.021.

Forbes, J. M. (1978), Tidal variations in thermospheric O, O_2, N_2, Ar, He, and H, *J. Geophys. Res.*, *83*(A8), 3691–3698, doi:10.1029/JA083iA08p03691.
Forbes, J. M., and D. Wu (2006), Solar tides as revealed by measurements of mesosphere temperature by the MLS experiment on UARS, *J. Atmos. Sci.*, *63*(7), 1776–1797, doi:10.1175/JAS3724.1.
Forbes, J. M., R. G. Roble, and C. G. Fesen (1993), Acceleration, heating, and compositional mixing of the thermosphere due to upward propagating tides, *J. Geophys. Res.*, *98*(A1), 311–321, doi:10.1029/92JA00442.
Forbes, J. M., J. Russell, S. Miyahara, X. Zhang, M. Mlynczak, C. J. Mertens, and M. E. Hagan (2006), Troposphere-thermosphere tidal coupling as measured by the SABER instrument on TIMED during July–September 2002, *J. Geophys. Res.*, *111*, A10S06, doi:10.1029/2005JA011492.
Forbes, J. M., X. Zhang, S. Palo, J. Russell, C. J. Mertens, and M. Mlynczak (2008), Tidal variability in the ionospheric dynamo region, *J. Geophys. Res.*, *113*, A02310, doi:10.1029/2007JA012737.
Forbes, J. M., S. L. Bruinsma, X. Zhang, and J. Oberheide (2009), Surface-exosphere coupling due to thermal tides, *Geophys. Res. Lett.*, *36*(15), doi:10.1029/2009GL038748.
Friedman, J. S., X. Zhang, X. Chu, and J. M. Forbes (2009), Longitude variations of the solar semidiurnal tides in the mesosphere and lower thermosphere at low latitudes observed from ground and space, *J. Geophys. Res.*, *114*, D11114, doi:10.1029/2009JD011763.
Gardner, C. S., and A. Z. Liu (2010), Wave-induced transport of atmospheric constituents and its effect on the mesospheric Na layer, *J. Geophys. Res. Atmospheres*, *115*, D20302, doi:10.1029/2010JD014140.
Groves, G., and J. M. Forbes (1984), Equinox tidal heating of the upper atmosphere, *Planet. Space Sci.*, *32*(4), 447–456.
Groves, G., and J. M. Forbes (1985), Mean zonal and meridional accelerations and mean heating induced by solar tides for equinox and solstice conditions, *Planet. Space Sci.*, *33*(3), 283–293.
Hines, C. O. (1965), Dynamical heating of the upper atmosphere, *J. Geophys. Res.*, *70*(1), 177–183, doi:10.1029/JZ070i001p00177.
Holton, J. R. (1975), The dynamic meteorology of the stratosphere and mesosphere, in *Meteor. Monogr.*, vol. 15, chap. 2, pp. 27–38, Am. Meteorol. Soc., Boston, Mass.
Jones, M., Jr., J. M. Forbes, M. E. Hagan, and A. Maute (2014a), Impacts of vertically propagating tides on the mean state of the ionosphere-thermosphere system, *J. Geophys. Res. Space Physics*, *119*(3), 2197–2213, doi:10.1002/2013JA019744.
Jones, M., Jr., J. M. Forbes, and M. E. Hagan (2014b), Tidal-induced net transport effects on the oxygen distribution in the thermosphere, *Geophys. Res. Lett.*, *41*, 5272–5279, doi:10.1002/2014GL060698.
Knipp, D., L. Kilcommons, L. Hunt, M. Mlynczak, V. Pilipenko, B. Bowman, Y. Deng, and K. Drake (2013), Thermospheric damping response to sheath-enhanced geospace storms, *Geophys. Res. Lett.*, *40*(7), 1263–1267, doi:10.1002/grl.50197.
Kockarts, G. (1980), Nitric oxide cooling in the terrestrial thermosphere, *Geophys. Res. Lett.*, *7*(2), 137–140, doi:10.1029/GL007i002p00137.
Laštovička, J. (2013), Trends in the upper atmosphere and ionosphere: Recent progress, *J. Geophys. Res. Space Physics*, *118*(6), 3924–3935, doi:10.1002/jgra.50341.
Lei, J., J. P. Thayer, A. G. Burns, G. Lu, and Y. Deng (2010), Wind and temperature effects on thermosphere mass density response to the November 2004 geomagnetic storm, *J. Geophys. Res.*, *115*, A05303, doi:10.1029/2009JA014754.
Lei, J., J. P. Thayer, W. Wang, and R. L. McPherron (2011), Impact of CIR storms on thermosphere density variability during the solar minimum of 2008, *Sol. Phys.*, *274*(1), 427–437, doi:10.1007/s11207-010-9563-y.
Leonard, J. M., J. M. Forbes, and H. G. Born (2012), Impact of tidal density variability on orbital and reentry predictions, *Space Weather*, *10*(12), S12003, doi:10.1029/2012SW000842.
Li, X., W. Wan, Z. Ren, L. Liu, and B. Ning (2015), The variability of nonmigrating tides detected from TIMED/SABER observations, *J. Geophys. Res. Space Physics*, *120*, 10,793–10,808, doi:10.1002/2015JA021577.
Lindzen, R. S. (1967), Thermally driven diurnal tide in the atmosphere, *Q. J. R. Meteorol. Soc.*, *93*(395), 18–42, doi:10.1002/qj.49709339503.
Lindzen, R. S., and D. Blake (1970), Mean heating of the thermosphere by tides, *J. Geophys. Res.*, *75*(33), 6868–6871, doi:10.1029/JC075i033p06868.
Marsh, D., and R. Roble (2002), TIME-GCM simulations of lower-thermospheric nitric oxide seen by the halogen occultation experiment, *J. Atmos. Sol. Terr. Phys.*, *64*(8–11), 889–895, doi:10.1016/S1364-6826(02)00044-5.
Marsh, D. R., and J. M. Russell (2000), A tidal explanation for the sunrise/sunset anomaly in HALOE low-latitude nitric oxide observations, *Geophys. Res. Lett.*, *27*(19), 3197–3200, doi:10.1029/2000GL000070.
Mlynczak, M., et al. (2003), The natural thermostat of nitric oxide emission at 5.3 μm in the thermosphere observed during the solar storms of april 2002, *Geophys. Res. Lett.*, *30*(21), 2100, doi:10.1029/2003GL017693.
Mlynczak, M. G., et al. (2010), Observations of infrared radiative cooling in the thermosphere on daily to multiyear timescales from the TIMED/SABER instrument, *J. Geophys. Res.*, *115*, A03309, doi:10.1029/2009JA014713.
Mlynczak, M. G., L. A. Hunt, C. J. Mertens, B. T. Marshall, J. M. Russell, T. Woods, R. E. Thompson, and L. L. Gordley (2014), Influence of solar variability on the infrared radiative cooling of the thermosphere from 2002 to 2014, *Geophys. Res. Lett.*, *41*(7), 2508–2513, doi:10.1002/2014GL059556.
Mukhtarov, P., D. Pancheva, and B. Andonov (2009), Global structure and seasonal and interannual variability of the migrating diurnal tide seen in the SABER/TIMED temperatures between 20 and 120 km, *J. Geophys. Res.*, *114*, A02309, doi:10.1029/2008JA013759.
Nguyen, V., and S. E. Palo (2014), Transmission of planetary wave effects to the upper atmosphere through eddy diffusion modulation, *J. Atmos. Sol. Terr. Phys.*, *117*, 1–6, doi:10.1016/j.jastp.2014.04.008.
Oberheide, J., and J. M. Forbes (2008), Thermospheric nitric oxide variability induced by nonmigrating tides, *Geophys. Res. Lett.*, *35*, L16814, doi:10.1029/2008GL034825.
Oberheide, J., M. E. H. R. G. Roble, and D. Offermann (2002), Sources of nonmigrating tides in the tropical middle atmosphere, *J. Geophys. Res.*, *107*(D21), 4567, doi:10.1029/2002JD002220.
Oberheide, J., J. M. Forbes, K. Häusler, Q. Wu, and S. L. Bruinsma (2009), Tropospheric tides from 80 to 400 km: Propagation, interannual variability, and solar cycle effects, *J. Geophys. Res.*, *114*, D00I05, doi:10.1029/2009JD012388.
Oberheide, J., J. M. Forbes, X. Zhang, and S. L. Bruinsma (2011a), Wave-driven variability in the ionosphere-thermosphere-mesosphere system from TIMED observations: What contributes to the "wave 4"?, *J. Geophys. Res.*, *116*, A01306, doi:10.1029/2010JA015911.
Oberheide, J., J. M. Forbes, X. Zhang, and S. L. Bruinsma (2011b), Climatology of upward propagating diurnal and semidiurnal tides in the thermosphere, *J. Geophys. Res.*, *116*, A11306, doi:10.1029/2011JA016784.
Oberheide, J., M. G. Mlynczak, C. N. Mosso, B. M. Schroeder, B. Funke, and A. Maute (2013), Impact of tropospheric tides on the nitric oxide 5.3 μm infrared cooling of the low-latitude thermosphere during solar minimum conditions, *J. Geophys. Res. Space Physics*, *118*, 7283–7293, doi:10.1002/2013JA019278.
Oliver, W. L., S. R. Zhang, and L. P. Goncharenko (2013), Is thermospheric global cooling caused by gravity waves?, *J. Geophys. Res. Space Physics*, *118*, 3898–3908, doi:10.1002/jgra.50370.

Pancheva, D., P. Mukhtarov, and B. Andonov (2010), Global structure, seasonal and interannual variability of the eastward propagating tides seen in the SABER/TIMED temperatures (2002–2007), *Adv. Space Res.*, *46*(3), 257–274, doi:10.1016/j.asr.2010.03.026.

Prölss, G. W. (2011), Density perturbations in the upper atmosphere caused by the dissipation of solar wind energy, *Surv. Geophys.*, *32*(2), 101–195, doi:10.1007/s10712-010-9104-0.

Qian, L. (2013), *The NCAR TIE-GCM: A Community Model of the Coupled Thermosphere/Ionosphere System*, edited by J. Huba, R. Schunk, and G. Khazanov, John Wiley, Ltd., pp. 73–83, Chichester, U. K.

Ren, Z., W. Wan, L. Liu, and J. Xiong (2011), Simulated longitudinal variations in the lower thermospheric nitric oxide induced by nonmigrating tides, *J. Geophys. Res.*, *116*, A04301, doi:10.1029/2010JA016131.

Richmond, A. D., and A. Maute (2014), *Ionospheric Electrodynamics Modeling*, 57–71, John Wiley, Ltd.

Richmond, A. D., E. C. Ridley, and R. G. Roble (1992), A thermosphere/ionosphere general circulation model with coupled electrodynamics, *Geophys. Res. Lett.*, *19*(6), 601–604, doi:10.1029/92GL00401.

Roble, R. G. (1995), *Energetics of the Mesosphere and Thermosphere*, edited by R. M. Johnson and T. L. Killeen, 1–21, AGU, Washington, D. C.

Roble, R. G., and E. C. Ridley (1987), An auroral model for the NCAR thermospheric general circulation model (TGCM), *Ann. Geophys.*, *5A*(6), 369–382.

Roble, R. G., E. C. Ridley, and R. E. Dickinson (1987), On the global mean structure of the thermosphere, *J. Geophys. Res.*, *92*(A8), 8745–8758, doi:10.1029/JA092iA08p08745.

Roble, R. G., E. Ridley, A. D. Richmond, and R. E. Dickinson (1988), A coupled thermosphere/ionosphere general circulation model, *Geophys. Res. Lett.*, *15*(12), 1325–1328, doi:10.1029/GL015i012p01325.

Siskind, D. E., C. A. Barth, and R. G. Roble (1989), The response of thermospheric nitric oxide to an auroral storm: 1. Low and middle latitudes, *J. Geophys. Res.*, *94*(A12), 16,885–16,898, doi:10.1029/JA094iA12p16885.

Siskind, D. E., C. A. Barth, and D. D. Cleary (1990), The possible effect of solar soft X rays on thermospheric nitric oxide, *J. Geophys. Res.*, *95*(A4), 4311–4317, doi:10.1029/JA095iA04p04311.

Siskind, D. E., J. M. Picone, M. H. Stevens, and K. Minschwaner (2004), Middle and upper thermospheric odd nitrogen: 1. A new analysis of rocket data, *J. Geophys. Res.*, *109*, A01303, doi:10.1029/2003JA009943.

Siskind, D. E., D. P. Drob, K. F. Dymond, and J. P. McCormack (2014), Simulations of the effects of vertical transport on the thermosphere and ionosphere using two coupled models, *J. Geophys. Res. Space Physics*, *119*, 1172–1185, doi:10.1002/2013JA019116.

Smith, A. K., D. R. Marsh, M. G. Mlynczak, and J. C. Mast (2010), Temporal variations of atomic oxygen in the upper mesosphere from SABER, *J. Geophys. Res. Atmos.*, *115*, D18309, doi:10.1029/2009JD013434.

Solomon, S. C., C. A. Barth, and S. M. Bailey (1999), Auroral production of nitric oxide measured by the SNOE satellite, *Geophys. Res. Lett.*, *26*(9), 1259–1262, doi:10.1029/1999GL900235.

Talaat, E. R., and R. S. Lieberman (1999), Nonmigrating diurnal tides in mesospheric and lower-thermospheric winds and temperatures, *J. Atmos. Sci.*, *56*(24), 4073–4087, doi:10.1175/1520-0469(1999)056<4073:NDTIMA>2.0.CO;2.

Truskowski, A. J., J. M. Forbes, X. Zhang, and S. E. Palo (2014), New perspectives on thermosphere tides: 1. Lower-thermosphere spectra and seasonal-latitudinal structures, *Earth, Planets and Space*, *66*, 136, doi:10.1186/s40623-014-0136-4.

Wang, W. (1998), A thermosphere-ionosphere nested grid (TING) model, PhD Thesis, Univ. Michigan.

Xu, J., A. K. Smith, H.-L. Liu, W. Yuan, Q. Wu, G. Jiang, M. G. Mlynczak, J. M. Russell, and S. J. Franke (2009), Seasonal and quasi-biennial variations in the migrating diurnal tide observed by Thermosphere, Ionosphere, Mesosphere, Energetics and Dynamics (TIMED), *J. Geophys. Res.*, *114*, D13107, doi:10.1029/2008JD011298.

Yamazaki, Y., and A. D. Richmond (2013), A theory of ionospheric response to upward-propagating tides: Electrodynamic effects and tidal mixing effects, *J. Geophys. Res. Space Physics*, *118*(9), 5891–5905, doi:10.1002/jgra.50487.

Zhang, X., J. M. Forbes, M. E. Hagan, J. M. Russell, S. E. Palo, C. J. Mertens, and M. G. Mlynczak (2006), Monthly tidal temperatures 20–120 km from TIMED/SABER, *J. Geophys. Res.*, *111*, A10S08, doi:10.1029/2005JA011504.

Zhang, X., J. M. Forbes, and M. E. Hagan (2010a), Longitudinal variation of tides in the MLT region: 1. Tides driven by tropospheric net radiative heating, *J. Geophys. Res.*, *115*, A06316, doi:10.1029/2009JA014897.

Zhang, X., J. M. Forbes, and M. E. Hagan (2010b), Longitudinal variation of tides in the MLT region: 2. Relative effects of solar radiative and latent heating, *J. Geophys. Res.*, *115*, A06317, doi:10.1029/2009JA014898.